RSC Advances

PAPER

View Article Online
View Journal | View Issue

Cite this: *RSC Adv.*, 2023, **13**, 6606

Hierarchical hollow tubular fibrous brucite-templated carbons obtained by KOH activation for supercapacitors†

Fangfang Liu, [ab] Xiuyun Chuan*[a] and Yupeng Zhao[a]

Hierarchical hollow tubular porous carbons have been widely used in applications of supercapacitors, batteries, CO_2 capture and catalysis due to their hollow tubular morphology, large aspect ratio, abundant pore structure and superior conductivity. Herein, hierarchical hollow tubular fibrous brucite-templated carbons (AHTFBC$_s$) were prepared using natural mineral fiber brucite as the template and KOH as the chemical activator. The effects of different KOH additions on the pore structure and capacitive performance of AHTFBC$_s$ were systematically studied. The specific surface area and micropore content of AHTFBC$_s$ after KOH activation were higher than those of HTFBC. The specific surface area of the HTFBC is 400 $m^2\ g^{-1}$, while the activated AHTFBC$_5$ has a specific surface area of up to 625 $m^2\ g^{-1}$. In particular, compared with HTFBC (6.1%), a series of AHTFBC$_s$ (22.1% for AHTFBC$_2$, 23.9% for AHTFBC$_3$, 26.8% for AHTFBC$_4$ and 22.9% for AHTFBC$_5$) with significantly increased micropore content were prepared by controlling the amount of KOH added. The AHTFBC$_4$ electrode displays a high capacitance of 197 F g^{-1} at 1 A g^{-1} and the capacitance retention of 100% after 10 000 cycles at 5 A g^{-1} in the three-electrode system. And an AHTFBC$_4$//AHTFBC$_4$ symmetric supercapacitor exhibits the capacitance of 109 F g^{-1} at 1 A g^{-1} in 6 M KOH and an energy density of 5.8 W h kg^{-1} at 199.0 W kg^{-1} in 1 M Na_2SO_4 electrolyte. In addition, the capacity retention of AHTFBC$_4$ in the symmetric supercapacitor was maintained at 92% after 5000 cycles in both 6 M KOH and 1 M Na_2SO_4 electrolytes.

Received 24th November 2022
Accepted 31st December 2022

DOI: 10.1039/d2ra07454k

rsc.li/rsc-advances

1. Introduction

With the over-exploitation of fossil energy and the deterioration of the ecological environment, the development of clean and renewable energy has become an important trend in today's society. Therefore, the effective development and utilization of renewable and clean energy, including wind energy, solar energy, *etc.*, has attracted the extensive attention of many scholars.[1] Therefore, there is an increasing demand for environmentally friendly, high-performance renewable energy storage devices.[2,3] As novel energy storage devices, supercapacitors (SC$_s$) have attracted much attention due to their high specific capacitance, long cycle life, high power density, safety, and no memory effect.[4–6]

Nanostructured carbon materials with high specific surface area (SSA) are commonly used electrode materials, which can provide high electrical conductivity, chemical stability, and electrochemical stability at a low cost.[7,8] Templated carbon is a widely used carbon-based material. At present, there are mainly "hard" template, "soft" template and the combination of "soft" and "hard" template used in the synthesis of template carbon material. The synthesis and final removal of hard templates undoubtedly increase the preparation cycle and preparation cost of template carbon, which restricts the large-scale application of the template method;[9] while soft templates cannot achieve the fine tuning of morphology and pore structure.[10] Therefore, based on the problems of soft and hard templates, natural minerals with unique nanopore structure, excellent thermal and mechanical stability, environmental friendliness, abundant resources and low cost have been widely concerned as templates. In recent years, a variety of natural minerals including chrysotile,[11] halloysite,[12] attapulgite,[13] sepiolite[14] (the above one-dimensional structure minerals), montmorillonite[15] (two-dimensional structure minerals), zeolite[16] and diatomite[17] (three-dimensional structure minerals) have been widely used as templates for the preparation of templated carbon materials.

Among various templated carbon materials, hollow tubular templated carbon is widely used due to its unique morphology, excellent chemical and mechanical stability and superior conductivity.[18,19] However, the limited accessible surface area of the closed tips and inert hydrophobic surfaces of hollow tubular templated carbon restricts its electrochemical performance.[20]

[a]*Key Laboratory of Orogen Belts and Crustal Evolution, School of Earth and Space Sciences, Peking University, Beijing 100871, China. E-mail: xychuan@pku.edu.cn*
[b]*School of Materials and Physics, China University of Mining and Technology, Xuzhou 221116, China*

† Electronic supplementary information (ESI) available. See DOI: https://doi.org/10.1039/d2ra07454k

Currently, in order to increase the specific capacitance and energy density of hollow tubular templated carbon materials without sacrificing high power density, there are usually two strategies, one is to design and build heteroatom-doped (such as B,[21] N,[22,23] P,[24] S[25]) structures, and the other is to build well-developed hierarchical pore structures. The introduction of heteroatoms into carbon materials not only improves the conductivity and wettability, but also provides more active sites and additional pseudocapacitance, thus significantly enhancing the electrochemical properties.[26] In addition to the doping of carbon materials with heteroatoms, the regulation of the pore structure of carbon materials has also aroused great interest in realizing the excellent properties of carbon materials. Generally speaking, during charge storage, macropores (>50 nm) can store electrolyte ions and act as electrolyte ion pools.[27] Mesopores (2–50 nm) are important bridges for the formation of three-dimensional ion transport channels inside the porous carbon material.[28] The existence of mesopores is conducive to the transport of electrolyte ions in the porous carbon material and improves the rate capability of porous carbon materials.[29,30] Micropores (size <2 nm) are the main contributor to the electric double-layer capacitance.[31,32] Therefore, the preparation of hierarchical porous carbon electrode materials with micropores, mesopores, and macropores is the key to ensuring the excellent electrochemical properties of SC_s.[31,33]

The activation method is currently one of the most common methods for preparing hierarchical porous carbons and can be divided into physical activation and chemical activation according to the pore-forming mechanism.[34] Compared with physical activation methods, chemical activation can achieve the preparation of hierarchical porous carbons at lower temperatures and higher yields, which has attracted much attention. Common chemical activators include strong bases such as KOH and NaOH, alkali metal compounds such as Na_2CO_3 and K_2CO_3, and Lewis acids such as $AlCl_3$, $ZnCl_2$, and H_3PO_3.[27] A literature survey shows that KOH is one of the most widely used active agents, and its product has a high SSA, so we choose KOH for chemical activation.[35]

Fibrous brucite ($Mg(OH)_2$) is the important non-metallic mineral resources, which presents one-dimensional fibrous, due to its fiber reinforcing properties and composition is widely used in fire retardant, paper making, extraction of magnesium oxide and magnesium chloride and environmental protection. However, the application of its nano-properties is less studied, therefore, in this paper, we choose fibrous brucite as a template to explore its application in the field of energy storage. In this work, we used the natural mineral fibrous brucite as the template and glucose as the carbon source to obtain hollow tubular template carbon material (HTFBC) through high temperature carbonization. Then, the activated fibrous brucite template carbon (AHTFBC) was prepared by controlling different KOH/carbon ratios at 800 °C for 2 h. $AHTFBC_s$ well inherit the one-dimensional structure of fibrous brucite, showing a hollow tubular structure. Secondly, compared with HTFBC, $AHTFBC_s$ have higher micropore content and excellent capacitance performance. $AHTFBC_4$ has a high specific capacitance of 197 F g^{-1} at 1 A g^{-1} in the three-electrode system.

2. Experiment

2.1 Materials

Fibrous brucite (FB) was provided by Shaanxi Tianbao Mining Co., Ltd. (Shanxi provinces, China); Dioctyl sulfosuccinate sodium salt (OT, ≥73.8%) and glucose (≥99%) were purchased from Sinopharm Chemical Reagent Co., Ltd.; hydrochloric acid (HCl, 36%), potassium hydroxide (KOH, ≥85%) and N-Methylpyrrolidone (NMP, 99.89%) were purchased from Xilong Science Co., Ltd.; anhydrous ethanol was purchased from Modern Oriental (Beijing) Technology Development Co., Ltd; Sodium sulfate (Na_2SO_4, 99%) was purchased from Beijing Tong Guang fine chemicals company; polyvinylidene fluoride (PVDF, 99.95%), conductive agent (acetylene black, 99.95%) and polytetrafluoroethylene emulsion (PTFE, 60 wt%) were purchased from cyber electrochemical materials network.

2.2 Fibrous brucite

FB was gray-white powder to the naked eye (Fig. S1a†), and it showed a fiber bundle of multiple fibers gathered together under an optical microscope (Fig. S1b†). Before the experiment, the raw ore was dispersed by a combination of chemical dispersion (dioctyl sulfosuccinate sodium salt (OT) as dispersant) and mechanical dispersion (stirring and ultrasonic), so that the fiber bundles were opened and divided into single fiber. The microscopic morphology of the dispersed FB was shown in Fig. S1c–d.† From the SEM and TEM image, it can be seen that the FB is in the form of one-dimensional fibers and the fibers are stacked and interlaced in a network structure. And the diameter of FB is about 50 nm. In order to further characterize the pore structure of FB, nitrogen adsorption–desorption tests were performed to characterize the specific surface area and pore size distribution. Fig. S1e† shows the nitrogen adsorption–desorption isotherm and the corresponding DFT pore size distribution of FB (Fig. S1f†). The nitrogen adsorption–desorption isotherm belongs to type IV adsorption isotherm, which indicates that it contains more mesopores. At low relative pressure, the adsorption volume is small and the adsorption isotherm rises slowly, indicating the presence of a small number of micropores. The pore structure information such as specific surface area and pore volume is shown in Table S1.† It can be seen that specific surface area (33 m^2 g^{-1}) and the percentage of micropores (around 1%) is very small.

2.3 Synthesis of hollow tubular fibrous brucite-templated carbons

First, fibrous brucite (2 g) and glucose (4 g) were added to 100 mL of deionized water, and a homogeneous mixture was obtained after stirring (6 h) and ultrasonic dispersion (1 h). The mixture was stirred in an oil bath at 110 °C for 8 h, and then the mixture was placed in an oven at 110 °C for 10 h to obtain the precursor. The dried samples were placed in a tube furnace and kept at 800 °C for 4 h in an Ar (5 °C min^{-1}).[36] After the temperature dropped to room temperature, 1 mol L^{-1} HCl solution was added to the sample, stirred for 24 h to remove the template, then washed with deionized water and ethanol

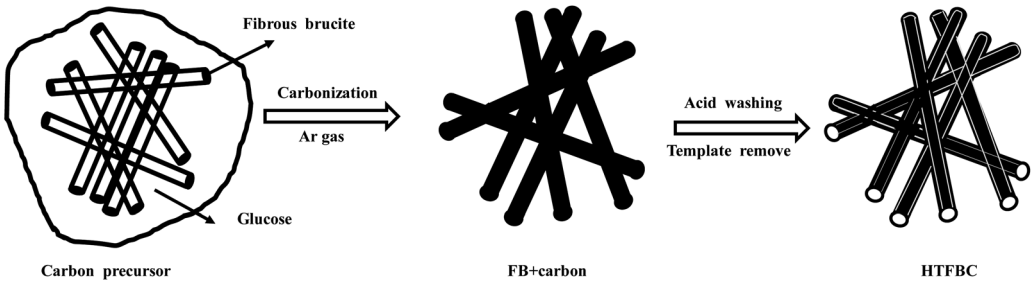

Fig. 1 Schematic illustration of the synthesis of the hollow tubular fibrous brucite-template carbon (HTFBC) using fibrous brucite as template.

successively, and dried at 110 °C to obtain the template carbon (HTFBC) (Fig. 1).

2.4 Synthesis of activated hollow tubular fibrous brucite-templated carbons

0.2 g KOH and 0.15 g of the fibrous brucite template carbon obtained in the previous step were ultrasonically dispersed in 20 mL deionized water and then dried in an oven at 110 °C overnight. The obtained mixture was placed in a tube furnace in an Ar and activated at 800 °C for 2 h (5 °C min^{-1}).[37–39] After the temperature dropped to room temperature, 1 mol L^{-1} HCl solution was added to the activated sample, stirred for 12 h to remove remaining KOH and by-products generated during the activation process, then washed with deionized water and ethanol until the solution became neutral, and finally dried at 110 °C to obtain activated fibrous brucite template carbon ($AHTFBC_2$) (Fig. 2). According to the mass ratio of KOH and template carbon of 0.3 : 0.15, 0.4 : 0.15 and 0.5 : 0.15, the obtained samples were labeled as $AHTFBC_3$, $AHTFBC_4$, and $AHTFBC_5$, respectively.

2.5 Characterizations

Optical mineralogy analysis of fibrous brucite was carried out using polarizing microscope (Nikon ECLIPSE LV100POL, Japan). The microscopic morphologies of fibrous brucite and template carbon materials were characterized by Nova Nano SEM 430

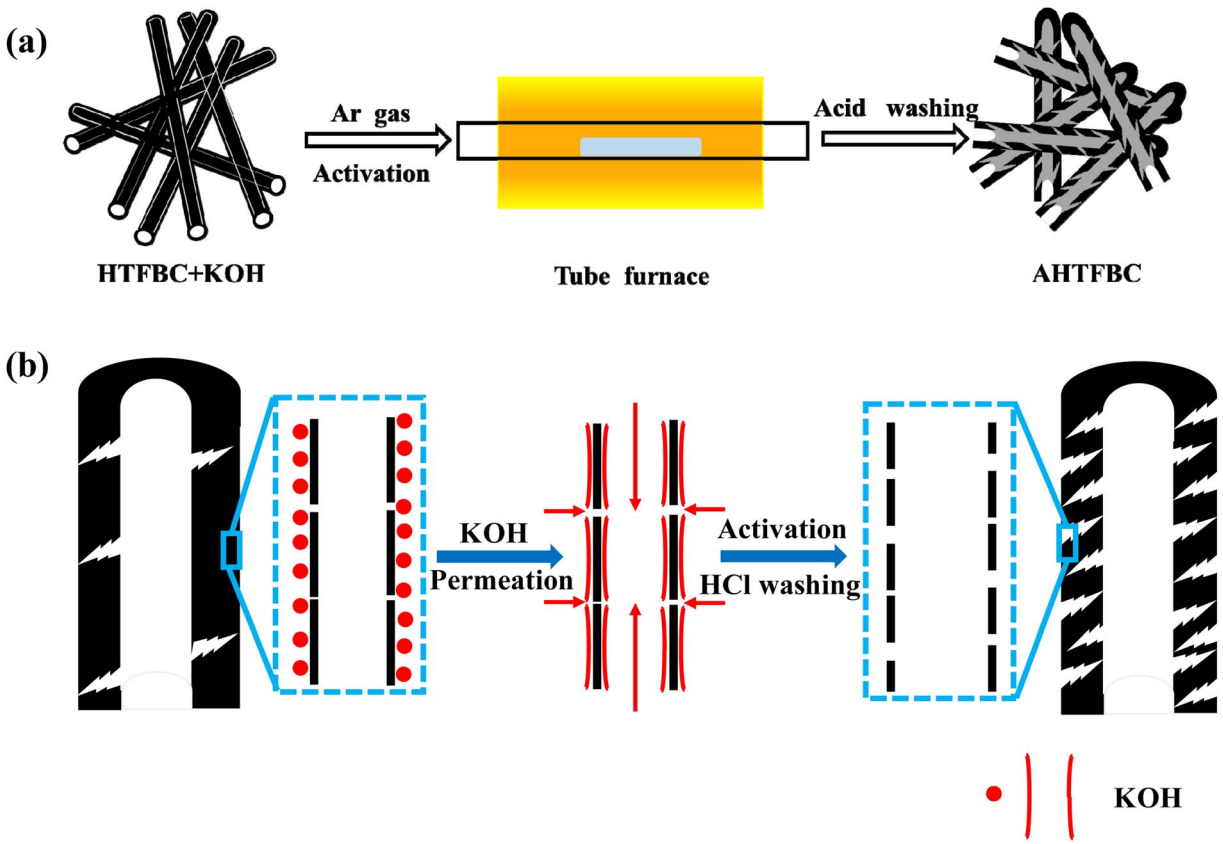

Fig. 2 Schematic representation of (a) KOH activated hollow tubular fibrous brucite-template carbon materials ($AHTFBC_s$) and (b) enlarged view of a single template carbon.

scanning electron microscope (FEI, USA, 15 kV, 176 μA) and TALOS F200X transmission electron microscope (FEI, USA, 200 kV, >150 μA). X-ray diffraction (XRD) was tested by X-ray diffractometer (Rigaku D/MAX-2400 PC, Japan) using Cu Kα (λ = 0.154 nm), with a scanning range of 5° to 75° and a scanning speed of 6°/min. The pore structure of template carbon materials was carried out with ASAP2010 nitrogen adsorption–desorption tester (Micrometer, USA), degassed at 120 °C for 12 h before the test, and the test temperature was −196 °C. Laser Raman analysis was performed using a Raman spectrometer (Micro-Raman-1000 high-resolution, Renishaw, UK) at a wavelength of 154 nm.

2.6 Electrode preparation and electrochemical measurements

In the three-electrode system, the Pt sheet and Hg/HgO were used as the counter electrode and reference electrode, respectively. Cyclic voltammograms (CV) (−0.8–0 V), galvanostatic charge–discharge (GCD) (−0.8–0 V), and electrochemical impedance spectroscopy (EIS) (0.1–10^5 Hz) tests were carried out on the working electrode in 6 mol L^{-1} KOH aqueous solution by CHI660E electrochemical workstation.

Preparation of working electrode: the prepared sample, conductive agent, and PTFE were mixed in a mass ratio of 8 : 1 : 1, and an appropriate amount of ethanol was added to the grind to obtain a viscous slurry. The slurry was uniformly coated on the foamed nickel current collector. After vacuum drying at 100 °C for 2 h, the working electrode was obtained by pressing with a hydraulic press (pressure 10 MPa). Put the pressed electrode sheet into 6 mol L^{-1} KOH solution, vacuum and infiltrate it in a vacuum dish for 0.5 h, and discharge the gas in the template carbon pores to obtain the final working electrode. According to the GCD curve, the single-electrode mass specific capacitance (C, F g^{-1}) of the active material is calculated by eqn (1):

$$C = I \cdot \Delta t / m \cdot \Delta U \quad (1)$$

where I (A) and Δt (s) are the discharge current and discharge time, respectively. m (g) is the mass of the active material of the working electrode, and ΔU (V) is the potential window during the discharge process.

In a two-electrode system, a 2032-type coin-type symmetrical capacitor was assembled with the prepared samples as the positive and negative electrodes, using 6 M KOH and 1 M Na_2SO_4 as the electrolytes, and glass fiber as the separator. GCD and CV measurements were performed on the CHI660E electrochemical workstation. The preparation method of symmetrical electrodes is similar to the above-mentioned three electrodes. The prepared materials, acetylene black and PVDF (mass ratio = 8 : 1 : 1) are uniformly dispersed in NMP and grinded to obtain a viscous slurry. It was coated on graphite paper, vacuum-dried at 100 °C for 2 h, and sliced to obtain the final electrode. According to the GCD curve, the specific capacitance (C_s, F g^{-1}) of a single electrode is calculated by the following eqn (2):

$$C_s = 4I\Delta t / m \cdot \Delta U \quad (2)$$

where I (A) and Δt (s) are the same as in the three-electrode system, m (g) is the total mass of the active material of the two electrodes, and ΔU (V) is the potential change excluding the IR drop. The energy density (E_t, W h kg^{-1}) and power density (P_t, W kg^{-1}) of the symmetrical supercapacitor were calculated by eqn (3) and (4), respectively:

$$E_t = C_t(\Delta U)2/2 \times 3.6 \quad (3)$$

$$P_t = E_t \times 3600/\Delta t \quad (4)$$

where C_t (F g^{-1}) is the specific capacitance of the total symmetrical supercapacitor, ΔU (V) is the cell voltage excluding the IR drop, and Δt (s) is the discharge time.

3. Results and discussion

3.1 Structure analysis

There are two broad peaks around 21° and 43°, corresponding to the (002) and (100) plane of the amorphous carbon in the XRD patterns of HTFBC and AHTFBC$_s$ (Fig. 3a), respectively.[8]

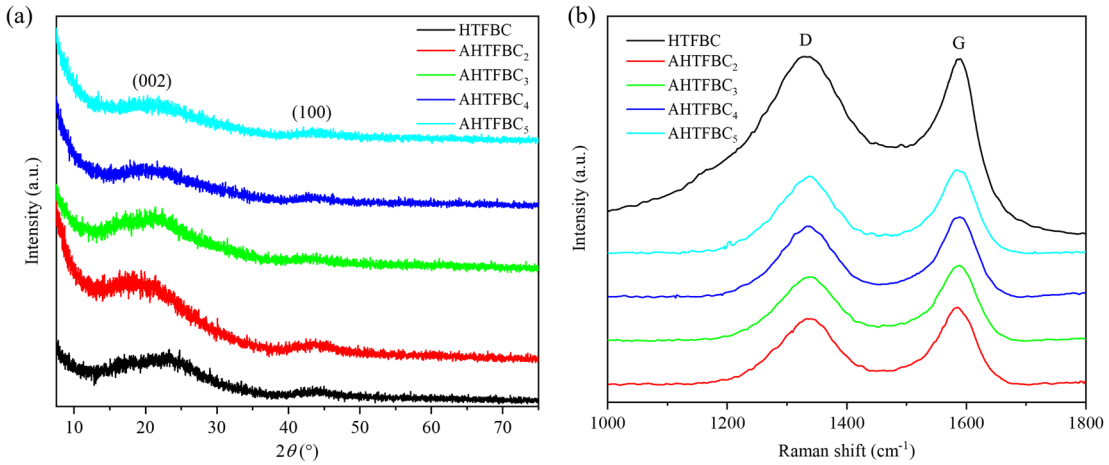

Fig. 3 (a) XRD patterns and (b) Raman spectra of HTFBC and AHTFBC$_s$.

Except for the diffraction peaks of amorphous carbon, there are no other diffraction peaks in the XRD patterns. It shows that the by-products generated during the activation process are completely removed. As can be seen from the Fig. 3a, the diffraction peak corresponding to the (002) crystalline plane of the activated $AHTFBC_s$ is significantly shifted to the left, indicating that the crystalline plane spacing of $AHTFBC_s$ has increased. Fig. 3b displays the Raman spectra of HTFBC and $AHTFBC_s$, and the peaks near 1336 cm^{-1} and 1583 cm^{-1} corresponding to the D band (disordered carbon or defective graphitic structures) and the G band (graphitic nature of carbon) respectively.[40] In addition, the intensity ratio of the D-band and G-band (I_D/I_G) were used to evaluate the graphitization degree of HTFBC and $AHTFBC_s$.[41,42] The I_D/I_G of HTFBC was 1.01, which was higher than those of the activated $AHTFBC_s$, indicating that defects of the HTFBC were removed after high temperature KOH activation.

3.2 Morphology analysis

In order to compare the effect of KOH activation on the morphology of porous carbon materials, we also observed the

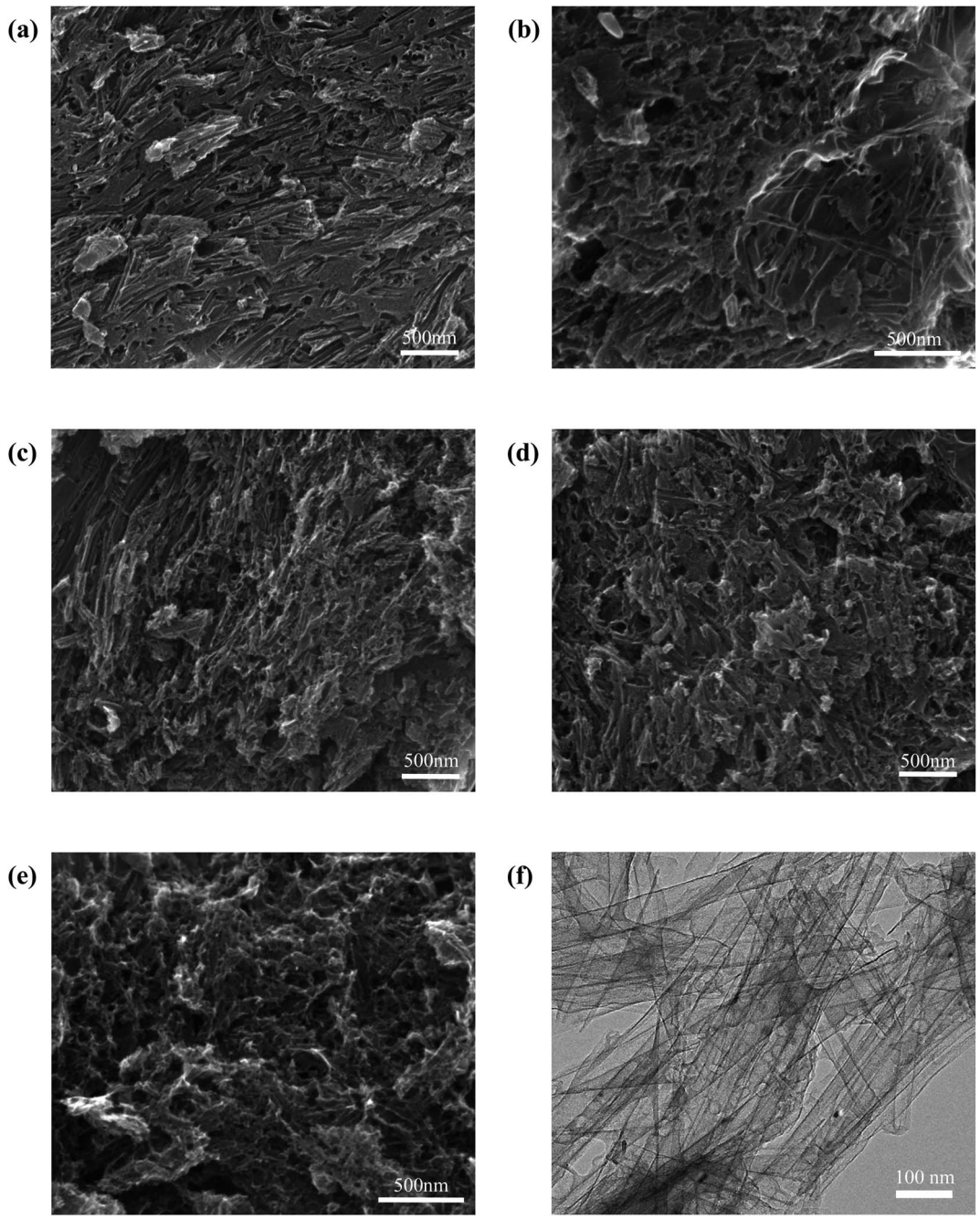

Fig. 4 Morphology of HTFBC and $AHTFBC_s$. SEM images of (a) HTFBC; (b) $AHTFBC_2$; (c) $AHTFBC_3$; (d) $AHTFBC_4$; (e) $AHTFBC_5$; (f) TEM images of $AHTFBC_4$.

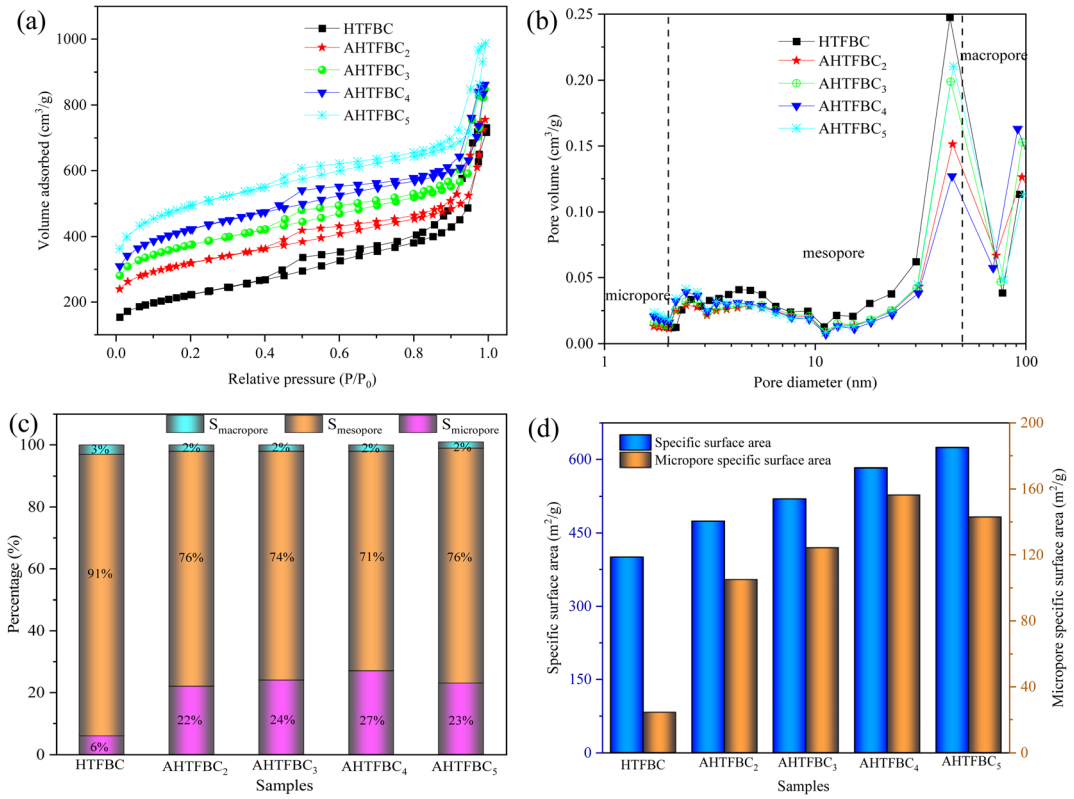

Fig. 5 (a) N_2 adsorption–desorption isotherms; (b) DFT pore size distribution; (c) percentage of the specific surface area of the three types of pore structure and (d) total and micropore specific surface area of HTFBC and AHTFBC$_s$.

morphology of unactivated template carbon (HTFBC), and the SEM image is shown in Fig. 4a. HTFBC displays carbon nanotubes that are heavily cross-linked and stacked together. Almost all the pores in the carbon material are contributed by hollow tubes, and there are basically no pores between the tubes, which may be formed by the direct carbonization of the excess carbon source in the voids between the templates.[43] Fig. 4b–e are SEM images of AHTFBC$_s$. It can be seen that compared to HTFBC, there are more pores inside AHTFBC$_s$ after KOH activation and etching. The appearance of a large number of pores facilitates the rapid transport of electrolyte ions and further improves the electrochemical performance of carbon materials.[44] The mass ratios of KOH and template carbon are controlled to be 0.2 : 0.15, 0.3 : 0.15, 0.4 : 0.15 and 0.5 : 0.15. Fig. 4b–e is the obtained SEM images of AHTFBC$_2$, AHTFBC$_3$, AHTFBC$_4$ and AHTFBC$_5$, respectively. With the increase of the KOH/carbon ratio, the pores inside AHTFBC$_s$ gradually increase, which is also consistent with the regularity of the SSA. The TEM image of AHTFBC$_4$ is shown in Fig. 4f. The inner diameter of the regular hollow tubular structure is about 50 nm, which is similar to the outer diameter of the FB template, indicating that the hollow template carbon inherits the one-dimensional structure of the template. It can be found in the TEM image of AHTFBC$_4$ that it is the hollow tubular structure, which is conducive to the rapid transport of electrolyte ions, thus enhancing the electrochemical performance.

3.3 Pore structure analysis

The pore structure of fibrous brucite template carbons before and after KOH activation was tested by nitrogen adsorption and desorption. As shown in Fig. 5a, both HTFBC and AHTFBC$_s$ adsorption and desorption isotherms belong to type IV curves.[45] The existence of hysteresis loops indicates that carbon materials have abundant mesopores.[46] In addition, at lower relative pressures (P/P_0 < 0.1), there were still adsorption amounts of HTFBC and AHTFBC$_s$, indicating that the samples contained micropores.[43] Fig. 5b shows that the pore size distribution of HTFBC and AHTFBC$_s$ is concentrated in mesopores (2–50 nm), and macropores (>50 nm), with a small amount of micropores. HTFBC and AHTFBC$_s$ exhibit a hierarchical porous structure, which facilitates the rapid transport of electrolyte ions.[46] The relative contents of SSA of the micropore, mesopore and macropore structures of HTFBC and AHTFBC$_s$ are shown in Fig. 5c. The micropore SSA of HTFBC accounted for 6.1% of the total SSA, while the AHTFBC$_s$ micropore SSA accounted for 22.1%, 23.9%, 26.8% and 22.9% of the total SSA, respectively. The micropore content increased significantly after activation, both increased by more than 2 times, and when the KOH: carbon mass ratio was 0.4 : 0.15, the obtained AHTFBC$_4$ had the highest micropore content. As the amount of KOH continued to increase, the content of micropores decreases, which is due to the excessive etching caused by excessive KOH, which causes the micropores collapse and connect into mesopores. From Fig. 5d and Table 1, it can be found that the SSA of AHTFBC$_s$

Table 1 Pore structures of HTFBC and AHTFBC$_s$

Samples	S_{total} ($m^2\ g^{-1}$)	S_{micro} ($m^2\ g^{-1}$)	S_{meso} ($m^2\ g^{-1}$)	S_{macro} ($m^2\ g^{-1}$)	V_{total} ($cm^3\ g^{-1}$)	V_{micro} ($cm^3\ g^{-1}$)	V_{meso} ($cm^3\ g^{-1}$)	V_{macro} ($cm^3\ g^{-1}$)	D_{ap} (nm)
HTFBC	400	24	365	11	0.91	0.01	0.63	0.27	4.5
AHTFBC$_2$	474	105	359	10	0.87	0.05	0.58	0.24	5.6
AHTFBC$_3$	520	124	386	10	0.94	0.06	0.64	0.24	4.8
AHTFBC$_4$	583	156	415	12	0.92	0.07	0.58	0.27	4.2
AHTFBC$_5$	625	143	472	10	1.02	0.07	0.70	0.25	3.6

after KOH activation is significantly increased compared with that of the HTFBC. The SSA of HTFBC was 400 $m^2\ g^{-1}$, and the SSA of activated AHTFBC$_2$, AHTFBC$_3$, AHTFBC$_4$, and AHTFBC$_5$ were 474, 520, 583 and 625 $m^2\ g^{-1}$, respectively. With the increase of KOH addition, the SSA of AHTFBCs shows a gradual increase, which is because the activator KOH will etch the internal pores of the template carbon, resulting in the increase in the micropore volume, which greatly increases the SSA of porous carbon. The micropore SSA of AHTFBC$_2$, AHTFBC$_3$, AHTFBC$_4$, and AHTFBC$_5$ were 105, 124, 156, and 143 $m^2\ g^{-1}$, respectively, which were significantly higher than that of the HTFBC (24 $m^2\ g^{-1}$). In addition, with the increase of KOH, the micropore SSA of AHTFBC$_s$ first increased and then decreased (Fig. 5d), of which AHTFBC$_4$ had the largest micropore SSA at 156 $m^2\ g^{-1}$. This is mainly because since with the increase of the amount of KOH added, a large number of micropores are generated by activation and etching in the pores of the template carbon material. However, when the amount of KOH is excessively added, the transitional etching will lead to the formation of micropores that are connected to form mesopores and even macropores. The reduction of micropores and micropore SSA will decrease the effective active sites inside the carbon materials, thereby affecting the electrochemical performance. Therefore, in the process of chemical activation, an appropriate KOH/carbon ratio should be selected so that the KOH-activated carbon material has hierarchical pore structure (suitable proportion of micropores, mesopores, and macropores).

3.4 Electrochemical properties analysis

The electrochemical properties of HTFBC and AHTFBC$_s$ were characterized by CV, GCD, and EIS in a three-electrode system, and the electrolyte was 6 M KOH solution. The voltammograms of HTFBC and AHTFBC$_s$ (Fig. 6a) display quasi-rectangular shapes at 100 mV s^{-1}, demonstrating good electric double-layer capacitance characteristics. Furthermore, the integral area of the CV curve of the AHTFBC$_s$ is larger than that of the HTFBC and AHTFBC$_4$ has the largest CV curve integral area. The CV curves of AHTFBC$_4$ (Fig. 6b) and other samples (Fig. S2†) present relatively regular rectangles at 5–100 mV s^{-1}, showing excellent rate performance and charge–discharge reversibility.[47,48] Fig. 6c compares the GCD curves of HTFBC and AHTFBC$_s$ at 1 A g^{-1}, and AHTFBC$_4$ exhibits the longest charge–discharge time. The GCD curves of HTFBC and AHTFBC$_s$ at 0.5–10 A g^{-1} (Fig. 6d and S3†) show good symmetry and linearity, indicating that they have excellent charge–discharge reversibility.[49] According to eqn (1) ($C_s = It/m\Delta U$), the specific capacitances of HTFBC and AHTFBC$_s$ before and after activation at 0.5–10 A g^{-1} are calculated as shown in Fig. 6e. At 1 A g^{-1}, the specific capacitance of HTFBC is 117 F g^{-1}, with the increase of KOH addition, the specific capacitance of AHTFBC$_s$ is 144, 158, 197 and 152 F g^{-1}, respectively, which are significantly larger than of HTFBC, indicating that the KOH activation can significantly improve the electrochemical properties of porous carbon. In addition, with the increase of the amount of KOH, the specific capacitance showed a trend of increasing first and then decreasing, which is due to the increased micropore content in the AHTFBC$_s$ after KOH activation and etching, which can increase more active sites for electrolyte ions, and therefore, the electrochemical properties are significantly improved. With the excess of KOH, the formed micropores will be further etched and connected into mesopores, which further affects its electrochemical performance. Among different KOH/carbon ratios, AHTFBC$_4$ has a maximum specific capacitance of 209 F g^{-1} at 0.5 A g^{-1}, the specific area of which are not the highest among the four AHTFBC$_s$ sample, indicating that the microporosity has the greatest influence on the electrochemical performance (Fig. S4†). The detailed comparison with the previous reported carbon nanotubes and hollow tubular carbons materials is listed in Table 2. The specific capacitance of AHTFBC$_4$ is higher than that reported commercially and laboratory prepared CNT, however, lower than that of the previously reported heteroatom-doped hollow tubular porous carbon. Therefore, the selection of suitable dopants for doping hollow tubular porous carbon is an effective strategy to improve its electrochemical properties.

Fig. S5† shows the cycling stability of HTFBC and AHTFBC$_4$ before and after activation. The capacity retention rate of both HTFBC and AHTFBC$_4$ samples after 10 000 charge–discharge cycles is 100%, exhibiting excellent cycling stability. Fig. 6f shows the Nyquist plots of HTFBC and AHTFBC$_s$ before and after activation. The Nyquist plots of HTFBC and four AHTFBC$_s$ samples show similar trends, which are all represented by the semicircle and straight lines. In the low-frequency region, HTFBC and AHTFBC$_s$ display an almost vertical-line characteristic, indicating that it has ideal electric double-layer capacitance behavior.[50] In the high-frequency region, the diameter of the semicircle represents the charge transfer resistance (R_{ct}).[51] The inset is the enlarged view of the high-frequency region and the fitted equivalent circuit diagram model. The R_{ct} value obtained by fitting HTFBC and AHTFBC$_s$ is 0.23, 0.24, 0.14, 0.15, and 0.31 Ω, respectively. The intercept of the Nyquist plots and

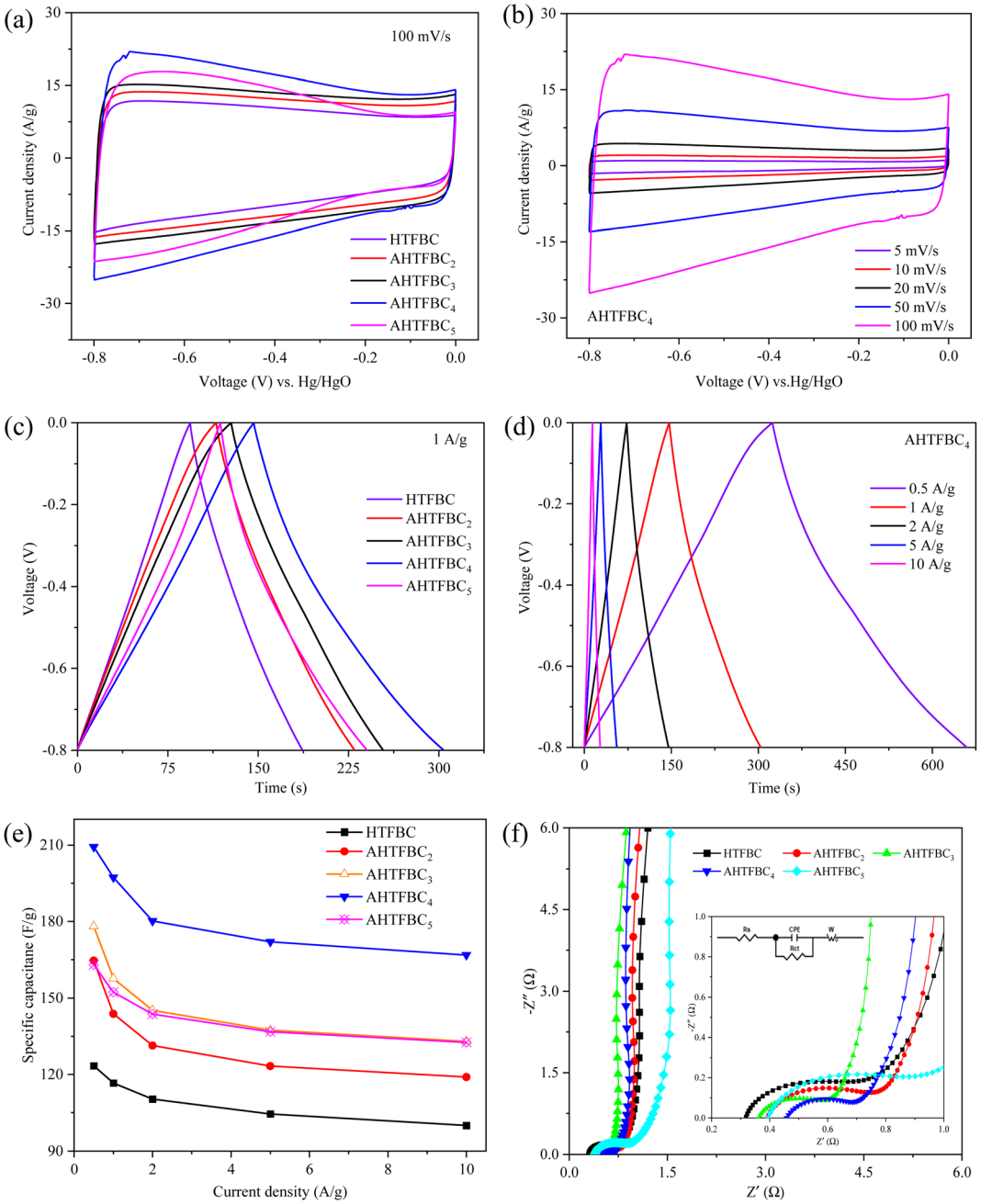

Fig. 6 Electrochemical properties of HTFBC and AHTFBC$_s$ in a three-electrode system. (a) CV curves at 100 mV s^{-1}; (b) CV curves of AHTFBC$_4$ at various scan rate; (c) GCD curves at 1 A g^{-1}; (d) GCD curves of AHTFBC$_4$ at 0.5–10 A g^{-1}; (e) specific capacitances; (f) Nyquist plots.

the Z′-axis corresponds to the equivalent series resistance (R_s),[52] represents the sum of the transport resistance of electrolyte ions in the electrolyte, the transport resistance of electrolyte ions in the electrode, and the interface resistance between the electrode and the electrolyte,[52,53] and the smaller the R_s of the porous carbon material, the better the conductivity.[51] The fitted R_s values of HTFBC and AHTFBC$_s$ are 0.31, 0.40, 0.36, 0.46, and 0.39 Ω, respectively. After activation, the R_s values of AHTFBC$_s$ are significantly greater than that of HTFBC, which may be due to the reduction of meso-porosity due to more micropores generated by KOH activation, thus affecting the transport of electrolyte ions in the pore structure.

A symmetrical two-electrode capacitor was assembled to further characterize the capacitive behavior of HTFBC and AHTFBC$_s$ in 6 M KOH. All the CV curves (Fig. 7a) at 100 mV s^{-1} for HTFBC, AHTFBC$_2$, AHTFBC$_3$, AHTFBC$_4$, and AHTFBC$_5$ samples display quasi-rectangular shapes, indicating their good double-layer capacitance characteristics. Furthermore, sample AHTFBC$_4$ has the largest integrated area of the CV curve. The CV curves of HTFBC and AHTFBC$_s$ with scan rates from 5 to 100 mV s^{-1} were shown in Fig. S6,† and it can be found that the shape of

Table 2 The comparison of electrochemical performance in this work with previous papers

Electrode material	Electrolyte	Heteroatom doping type	Activator	Specific surface area ($m^2\ g^{-1}$)	C_s ($F\ g^{-1}$)	Ref.
$AHTFBC_4$	6 M KOH	C	KOH	583	197 at 1 A g^{-1}	This work
N—CNTs	1 M KOH	N		—	150 at 0.5 A g^{-1}	54
NCNT-1	6 M KOH	N		80.2	205 at 20 mV s^{-1}	55
CNT	6 M KOH	—	—	271	45 at 1 A g^{-1}	56
CNT	6 M KOH	—	—	201	47 at 1 A g^{-1}	57
CNT	1 M $LiClO_4$	—	—	42.8	7 at 0.2 A g^{-1} (two)	58
MCNTs	6 M KOH	—	—	126	64 at 0.5 A g^{-1} (two)	59
CF-HPC-2	6 M KOH	N, O, S	$NaHCO_3$	516.7	349 F cm^{-3} at 1 A g^{-1}	60
B/N-PCTB	6 M KOH	B, N	KOH	1420	355 at 1 A g^{-1}	61
HT-PC	6 M KOH	O	KOH	637.1	315 at 1 A g^{-1}	62
HCMT-650	1 M $TEABF_4$/PC	N, P	$(NH_4)_2HPO_4$	1600	140.7 at 1 A g^{-1} (two)	63
HTPC	6 M KOH	O, P	$KOH–KNO_3$	1508	278 at 1 A g^{-1}	64
NMCT-2-800	6 M KOH	N, O, F	—	1071	269 at 0.5 A g^{-1}	65
N-MCT	6 M KOH	N, O, F	—	1334	349 at 0.5 A g^{-1}	66

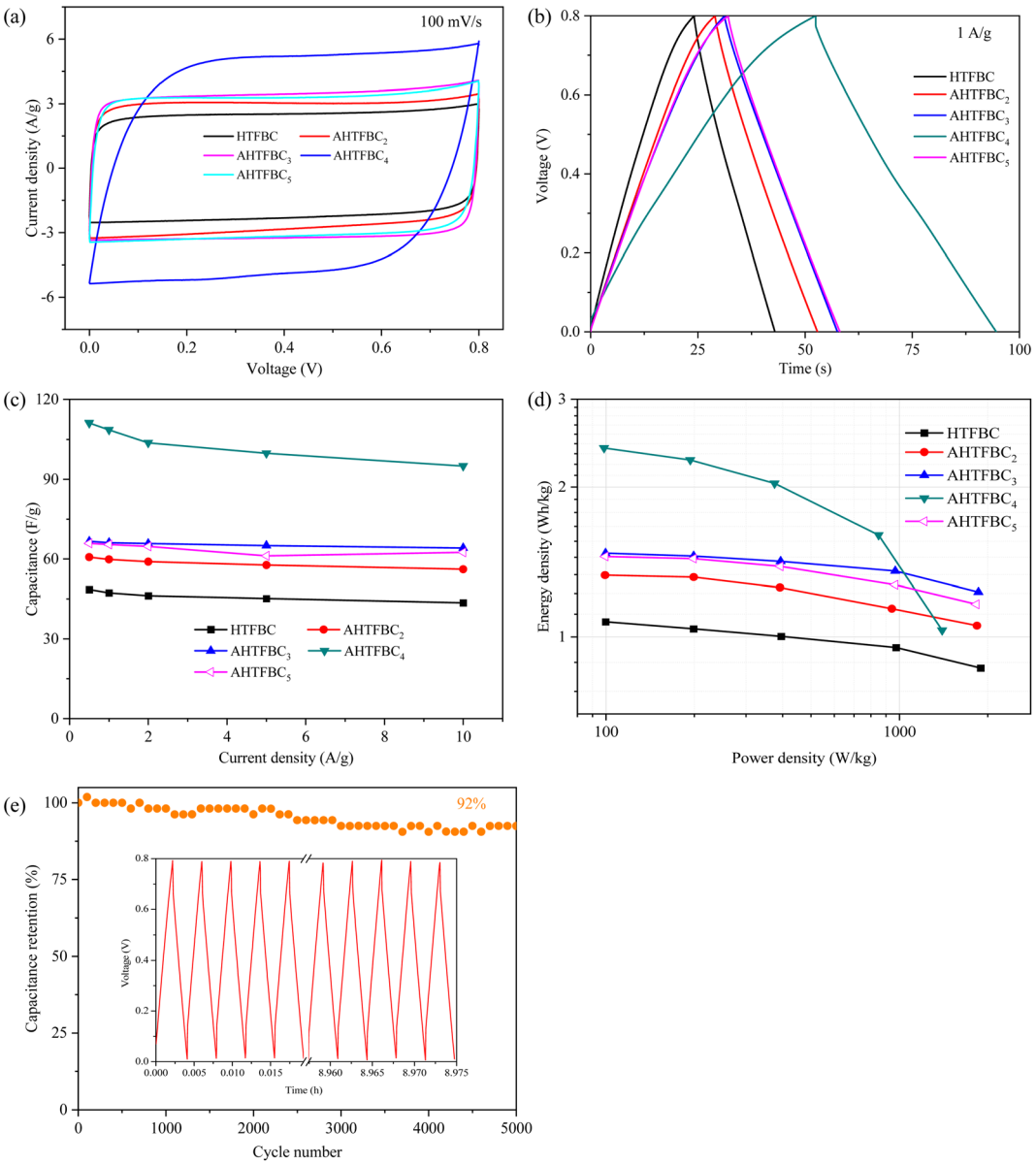

Fig. 7 Electrochemical properties of HTFBC//HTFBC and $AHTFBC_s$//$AHTFBC_s$ symmetric supercapacitors in the 6 M KOH electrolyte. (a) CV curves at 100 mV s^{-1}; (b) GCD curves at 1 A g^{-1}; (c) specific capacitances at 0.5–10 A g^{-1}; (d) Ragone plot; (e) cycling stability of $AHTFBC_4$ at 5 A g^{-1}.

the CV curves was hardly deformed as the scan rate increases, indicating the excellent rate performance of the samples. The GCD curves at 1 A g^{-1} (Fig. 7b) of HTFBC, AHTFBC$_2$, AHTFBC$_3$, AHTFBC$_4$, and AHTFBC$_5$ samples show approximately an isosceles triangle, indicating good charge–discharge reversibility. And sample AHTFBC$_4$ has the longest charge–discharge time. The GCD curves at 0.5–10 A g^{-1} display good linearity and exhibit a small IR drop, demonstrating good electrochemical performance (Fig. S7†). The capacitance is 47, 60, 66, 109, and 65 F g^{-1} at 1 A g^{-1} for HTFBC, AHTFBC$_2$, AHTFBC$_3$, AHTFBC$_4$, and AHTFBC$_5$, respectively (Fig. 7c). The Ragone plot showing the energy-power density correlation is shown in Fig. 7d. At 0.5 A g^{-1}, AHTFBC$_4$ represents a high energy density of 2.4 W h kg^{-1} at the power density of 98.5 W kg^{-1}, superior to HTFBC, AHTFBC$_2$, AHTFBC$_3$ and AHTFBC$_5$ with the energy density of 1.1 W h kg^{-1} at the power density of 99.7 W kg^{-1}, 1.3 W h kg^{-1} at 99.3 W kg^{-1}, 1.5 W h kg^{-1} at 99.7 W kg^{-1} and 1.5 W h kg^{-1} at 99.5 W kg^{-1}, respectively. In addition, the energy density of AHTFBC$_4$ maintains at 1.6 W h kg^{-1}, and when the power density increases to 849.6 W kg^{-1} at 5 A g^{-1}. The capacity retention of AHTFBC$_4$ remains at 92% after 5000 cycles at 5 A g^{-1} (Fig. 7e), suggesting good cycle performance.

Because the Na_2SO_4 electrolyte has a higher working voltage than the KOH electrolyte, Na_2SO_4 is also used as the electrolyte to assemble a symmetrical capacitor. Fig. 8a and S8† are the CV curves of HTFBC and AHTFBC$_s$. The GCD curves of HTFBC and AHTFBC$_s$ are shown in Fig. 8b and S9.† Both CV and GCD curves show that HTFBC and AHTFBC$_s$ electrodes have good electric

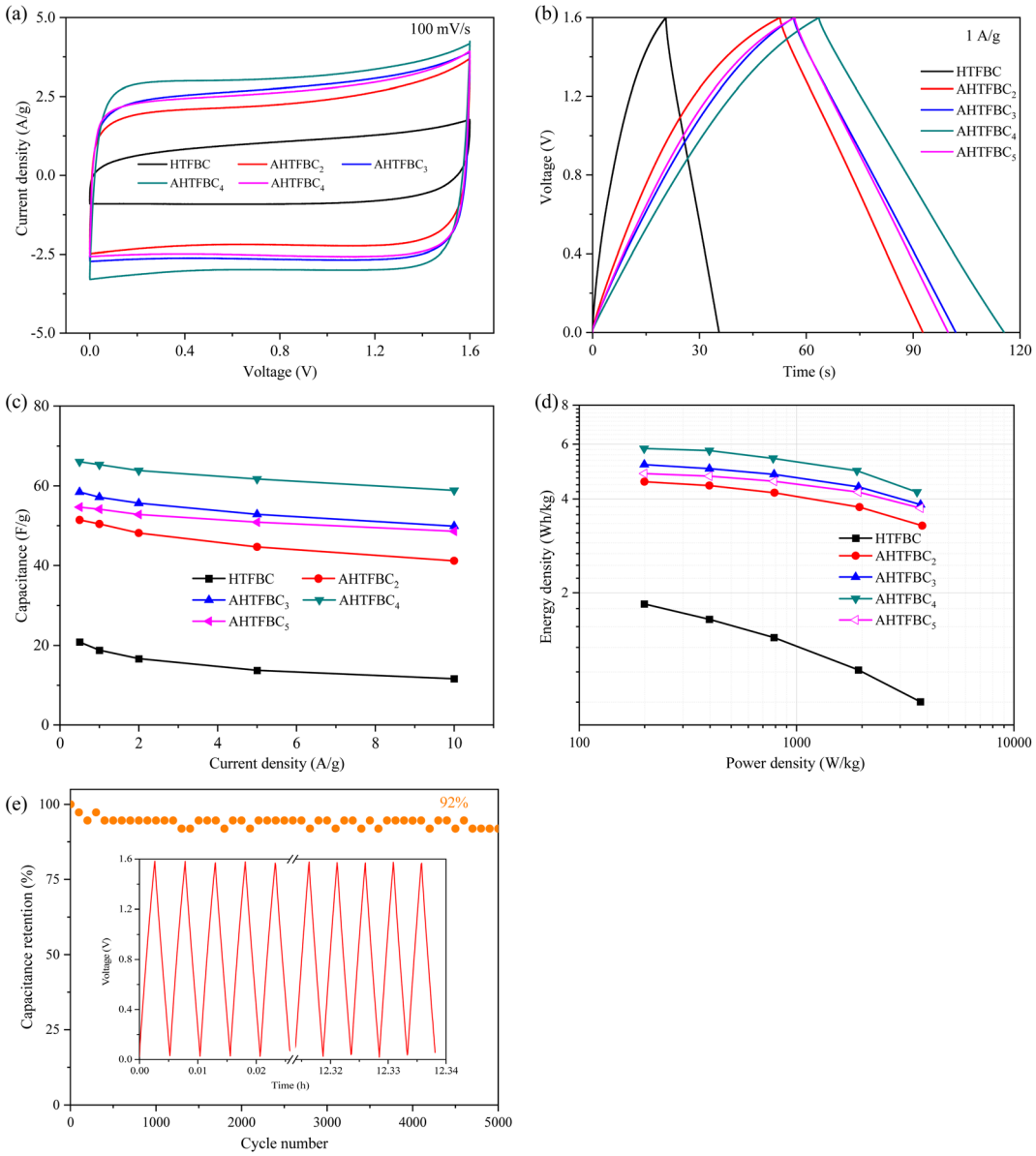

Fig. 8 Electrochemical properties of HTFBC//HTFBC and AHTFBC$_s$//AHTFBC$_s$ symmetric supercapacitors in the 1 M Na_2SO_4 electrolyte. (a) CV curves at 100 mV s^{-1}; (b) GCD curves at 1 A g^{-1}; (c) specific capacitances at 0.5–10 A g^{-1}; (d) Ragone plot; (e) cycling stability of AHTFBC$_4$ at 5 A g^{-1}.

double layer capacitive behavior. The specific capacitance value for $AHTFBC_s$ is significantly higher than that for HTFBC (Fig. 8c). At 1 A g^{-1}, the specific capacitance of HTFBC, $AHTFBC_2$, $AHTFBC_3$, $AHTFBC_4$, and $AHTFBC_5$ is 19, 50, 57, 65 and 54 F g^{-1}, respectively. In addition, the energy density of $AHTFBC_s$ is also significantly larger than that of HTFBC under the same power density (Fig. 8d). $AHTFBC_2$, $AHTFBC_3$, $AHTFBC_4$, and $AHTFBC_5$ show the energy density of 4.6 W h kg^{-1} at 199.5 W kg^{-1}, 5.2 W h kg^{-1} at 199.3 W kg^{-1}, 5.8 W h kg^{-1} at 199.0 W kg^{-1} and 4.8 W h kg^{-1} at 199.3 W kg^{-1}, which are more than twice that in the KOH electrolyte at similar power density (1.3 W h kg^{-1} at 99.3 W kg^{-1}, 1.5 W h kg^{-1} at 99.7 W kg^{-1}, 2.4 W h kg^{-1} at 98.5 W kg^{-1} and 1.5 W h kg^{-1} at 99.5 W kg^{-1}). Cycling stability was evaluated by GCD at 5 A g^{-1} up to 5000 cycles (Fig. 8e). The capacity retention of $AHTFBC_4$ remains at 92% after 5000 cycles.

4. Conclusions

In summary, as a one-dimensional fibrous structure, fibrous brucite is an ideal template for the preparation of hollow tubular porous carbon, and KOH activation has a great influence on the pore structure of porous carbon. In particular, the micropores generated during the activation process are important for improving the capacitive performance of porous carbons. In the three-electrode system, the $AHTFBC_4$ electrode displays a high specific capacitance of 197 F g^{-1} at 1 A g^{-1}, which is much higher than that of the HTFBC electrode of 117 F g^{-1}, resulting in more microporous channels due to KOH activation and etching. In addition, the symmetric two-electrode capacitor fabricated by $AHTFBC_4$ achieves an energy density of 5.8 W h kg^{-1} at 199.0 W kg^{-1} in 1 M Na_2SO_4 electrolyte, which is significantly higher than that of HTFBC of 1.8 W h kg^{-1} at 199 W kg^{-1}.

Conflicts of interest

There are no conflicts to declare.

Acknowledgements

The authors would like to acknowledge the support from National Natural Science Foundation of China (No.51774016 and No.52074015), Clinical Medicine Plus X–Young Scholars Project, Peking University, the Fundamental Research Funds for the Central Universities (33) and Test Fund of Peking University (0000012321).

References

1 S. J. Song, *et al.*, Facile self-templating large scale preparation of biomass-derived 3D hierarchical porous carbon for advanced supercapacitors, *J. Mater. Chem. A*, 2015, **3**, 18154–18162, DOI: **10.1039/c5ta04721h**.

2 X. Pu, *et al.*, Wearable Textile-Based In-Plane Microsupercapacitors, *Adv. Energy Mater.*, 2016, **6**, 1601254, DOI: **10.1002/aenm.201601254**.

3 M. He, *et al.*, Thermopower enhancement in conducting polymer nanocomposites *via* carrier energy scattering at the organic–inorganic semiconductor interface, *Energy Environ. Sci.*, 2012, **5**, 8351–8358, DOI: **10.1039/C2EE21803H**.

4 Y. Gu, *et al.*, Highly N/O co-doped ultramicroporous carbons derived from nonporous metal-organic framework for high performance supercapacitors, *Chin. Chem. Lett.*, 2021, **32**, 1491–1496, DOI: **10.1016/j.cclet.2020.09.029**.

5 X. L. Chen, R. Paul and L. M. Dai, Carbon-based supercapacitors for efficient energy storage, *Natl. Sci. Rev.*, 2017, **4**, 453–489, DOI: **10.1093/nsr/nwx009**.

6 C. Chen, *et al.*, Three-dimensional scaffolding framework of porous carbon nanosheets derived from plant wastes for high-performance supercapacitors, *Nano Energy*, 2016, **27**, 377–389, DOI: **10.1016/j.nanoen.2016.07.020**.

7 H. Jiang, P. S. Lee and C. Li, 3D carbon based nanostructures for advanced supercapacitors, *Energy Environ. Sci.*, 2013, **6**, 41–53, DOI: **10.1039/c2ee23284g**.

8 M. Song, *et al.*, Biowaste-based porous carbon for supercapacitor: The influence of preparation processes on structure and performance, *J. Colloid Interface Sci.*, 2019, **535**, 276–286, DOI: **10.1016/j.jcis.2018.09.055**.

9 J. Zhou, *et al.*, Nitrogen-doped hierarchical porous carbon materials prepared from meta-aminophenol formaldehyde resin for supercapacitor with high rate performance, *Electrochim. Acta*, 2015, **153**, 68–75, DOI: **10.1016/j.electacta.2014.11.075**.

10 J. Wang, *et al.*, Size-controlled nitrogen-containing mesoporous carbon nanospheres by one-step aqueous self-assembly strategy, *J. Mater. Chem. A*, 2015, **3**, 2305–2313, DOI: **10.1039/C4TA05820H**.

11 X. Cao, X. Y. Chuan, A. J. Li and D. B. Huang, Preparation of porous carbons using a chrysotile template and their electrochemical performance as supercapacitor electrodes, *New Carbon Mater.*, 2018, **33**, 229–236, DOI: **10.19869/j.ncm.1007-8827.2018.03.003**.

12 S. Zong, *et al.*, N-doped crumpled carbon nanotubes as advanced electrode material for supercapacitor, *J. Alloys Compd.*, 2022, **928**, 167222, DOI: **10.1016/j.jallcom.2022.167222**.

13 R. Li, *et al.*, Design and synthesis of tungsten trioxide/polypyrrole/graphene using attapulgite as template for high-performance supercapacitors, *Electrochim. Acta*, 2019, **311**, 123–131, DOI: **10.1016/j.electacta.2019.04.159**.

14 S. Yang, C. Li, Y. Li and P. Wu, Insight into the effect of clay mineral structure on clay-derived N-doped carbon materials and their efficient electrocatalytic performance, *Surf. Interfaces*, 2022, **31**, 102000, DOI: **10.1016/j.surfin.2022.102000**.

15 N. Y. W. Zaw, *et al.*, Clay-assisted hierarchical growth of metal-telluride nanostructures as an anode material for hybrid supercapacitors, *Appl. Clay Sci.*, 2022, **225**, 106539, DOI: **10.1016/j.clay.2022.106539**.

16 A. Policicchio, *et al.*, Large carbon dioxide adsorption in ZTC at medium pressure: Effects of surface functionalization, *Carbon*, 2023, **201**, 991–1000, DOI: **10.1016/j.carbon.2022.10.001**.

17 A. Li, *et al.*, Influence of Activated Condition on the Structure of Diatomite-templated Carbons and Their Electrochemical Properties as Supercapacitors, *Electrochemistry*, 2017, **85**, 708–714, DOI: 10.5796/electrochemistry.85.708.

18 D. Zhang, *et al.*, High performance of filter capacitor based on nitrogen-doped carbon nanotube supercapacitor, *Nanotechnology*, 2020, **31**, 495601, DOI: 10.1088/1361-6528/abb1ec.

19 S. Bayatpour, M. Afsharpour, Z. Dini and H. R. Naderi, High performance supercapacitor electrodes using functionalized CNTs/MoO3 with natural polysaccharide binders, *J. Mater. Sci.: Mater. Electron.*, 2020, **31**, 6150–6159, DOI: 10.1007/s10854-020-03168-2.

20 Y. Zhang, *et al.*, Template-free method for fabricating carbon nanotube combined with thin N-doped porous carbon composite for supercapacitor, *J. Mater. Sci.*, 2019, **54**, 6451–6460, DOI: 10.1007/s10853-018-03290-x.

21 Z.-X. Xu, *et al.*, DES mediated synthesis of sewage sludge-derived B, N-doped carbons for electrochemical applications, *Chemosphere*, 2022, **308**, 135840, DOI: 10.1016/j.chemosphere.2022.135840.

22 X. Zheng, *et al.*, In situ nanoarchitecturing of conjugated polyamide network-derived carbon cathodes toward high energy-power Zn-ion capacitors, *J. Mater. Chem. A*, 2022, **10**, 611–621, DOI: 10.1039/D1TA07350H.

23 Z. Song, *et al.*, Lewis Pair Interaction Self-Assembly of Carbon Superstructures Harvesting High-Energy and Ultralong-Life Zinc-Ion Storage, *Adv. Funct. Mater.*, 2022, **32**, 2208049, DOI: 10.1002/adfm.202208049.

24 Y. Rao, *et al.*, Laser-scribed phosphorus-doped graphene derived from Kevlar textile for enhanced wearable micro-supercapacitor, *J. Colloid Interface Sci.*, 2023, **630**, 586–594, DOI: 10.1016/j.jcis.2022.10.024.

25 F. F. Liu, X. Y. Chuan, Y. Yang and A. J. Li, Influence of N/S Co-doping on Electrochemical Property of Brucite Template Carbon Nanotubes, *J. Inorg. Mater.*, 2021, **36**, 711–717, DOI: 10.15541/jim20200033.

26 S. Park, J. Kim and K. Kwon, A review on biomass-derived N-doped carbons as electrocatalysts in electrochemical energy applications, *Chem. Eng. J.*, 2022, **446**, 137116, DOI: 10.1016/j.cej.2022.137116.

27 J. Yin, W. Zhang, N. A. Alhebshi, N. Salah and H. N. Alshareef, Synthesis Strategies of Porous Carbon for Supercapacitor Applications, *Small Methods*, 2020, **4**, 1900853, DOI: 10.1002/smtd.201900853.

28 M. B. Wu, *et al.*, Synthesis of starch-derived mesoporous carbon for electric double layer capacitor, *Chem. Eng. J.*, 2014, **245**, 166–172, DOI: 10.1016/j.cej.2014.02.023.

29 W. Xing, *et al.*, Hierarchical porous carbons with high performance for supercapacitor electrodes, *Carbon*, 2009, **47**, 1715–1722, DOI: 10.1016/j.carbon.2009.02.024.

30 J. Zhou, H. Wang, W. Yang, S. J. Wu and W. Han, Sustainable nitrogen-rich hierarchical porous carbon nest for supercapacitor application, *Carbohydr. Polym.*, 2018, **198**, 364–374, DOI: 10.1016/j.carbpol.2018.06.095.

31 J. Chmiola, *et al.*, Anomalous increase in carbon capacitance at pore sizes less than 1 nanometer, *Science*, 2006, **313**, 1760–1763, DOI: 10.1126/science.1132195.

32 D. P. Qiu, *et al.*, Kinetics Enhanced Nitrogen-Doped Hierarchical Porous Hollow Carbon Spheres Boosting Advanced Potassium-Ion Hybrid Capacitors, *Adv. Funct. Mater.*, 2019, **29**, 1903496, DOI: 10.1002/adfm.201903496.

33 S. Kondrat, C. R. Perez, V. Presser, Y. Gogotsi and A. A. Kornyshev, Effect of pore size and its dispersity on the energy storage in nanoporous supercapacitors, *Energy Environ. Sci.*, 2012, **5**, 6474–6479, DOI: 10.1039/c2ee03092f.

34 M. Sevilla and R. Mokaya, Energy storage applications of activated carbons: supercapacitors and hydrogen storage, *Energy Environ. Sci.*, 2014, **7**, 1250–1280, DOI: 10.1039/C3EE43525C.

35 S.-H. Yoon, *et al.*, KOH activation of carbon nanofibers, *Carbon*, 2004, **42**, 1723–1729, DOI: 10.1016/j.carbon.2004.03.006.

36 X. D. Yuan, *et al.*, Template Synthesis of Nitrogen Self-Doped Hierarchical Porous Carbon with Supermicropores and Mesopores for Electrical Double-Layer Capacitors, *Bioresources*, 2023, **18**, 87–99, DOI: 10.15376/biores.18.1.87-99.

37 Y. Wang, *et al.*, Ternary-doped hierarchical porous carbons derived from durian kernel as electrode materials for efficient energy storage devices, *Diamond Relat. Mater.*, 2022, **130**, 109451, DOI: 10.1016/j.diamond.2022.109451.

38 X. Wang, *et al.*, Controllable adjustment strategies for activated carbon and application in supercapacitors with both ultra-high capacitance and rate performance, *Diamond Relat. Mater.*, 2022, **130**, 109466, DOI: 10.1016/j.diamond.2022.109466.

39 X. Guo, X. Zhang, Y. Wang, X. Tian and Y. Qiao, Converting furfural residue wastes to carbon materials for high performance supercapacitor, *Green Energy Environ.*, 2022, **7**, 1270–1280, DOI: 10.1016/j.gee.2021.01.021.

40 S. S. Shah, *et al.*, Jute Sticks Derived and Commercially Available Activated Carbons for Symmetric Supercapacitors with Bio-electrolyte: A Comparative Study, *Synth. Met.*, 2021, **277**, 116765, DOI: 10.1016/j.synthmet.2021.116765.

41 J. Yan, *et al.*, High-energy aqueous supercapacitors enabled by N/O codoped carbon nanosheets and "water-in-salt" electrolyte, *Chin. Chem. Lett.*, 2022, **33**, 2681–2686, DOI: 10.1016/j.cclet.2021.08.123.

42 F. Liu, X. Chuan, B. Li and P. Qi, One-step carbonization synthesis of in-situ nitrogen-doped carbon tubes using fibrous brucite as the template for supercapacitors, *Mater. Chem. Phys.*, 2022, **281**, 125811, DOI: 10.1016/j.matchemphys.2022.125811.

43 L. Shi, *et al.*, Fabrication of hierarchical porous carbon microspheres using porous layered double oxide templates for high-performance lithium ion batteries, *Carbon*, 2017, **123**, 186–192, DOI: 10.1016/j.carbon.2017.07.062.

44 S. Song, *et al.*, Facile self-templating large scale preparation of biomass-derived 3D hierarchical porous carbon for advanced supercapacitors, *J. Mater. Chem. A*, 2015, **3**, 18154–18162, DOI: 10.1039/C5TA04721H.

45 C. Liu, *et al.*, Nitrogen-doped soft carbon frameworks built of well-interconnected nanocapsules enabling a superior potassium-ion batteries anode, *Chem. Eng. J.*, 2020, **382**, 121759, DOI: 10.1016/j.cej.2019.05.120.

46 M. Yang, Q. Kong, W. Feng, W. Yao and Q. Wang, Hierarchical porous nitrogen, oxygen, and phosphorus ternary doped hollow biomass carbon spheres for high-speed and long-life potassium storage, *Carbon Energy*, 2022, **4**, 45–59, DOI: 10.1002/cey2.157.

47 X. Fan, *et al.*, A Layered-Nanospace-Confinement Strategy for the Synthesis of Two-Dimensional Porous Carbon Nanosheets for High-Rate Performance Supercapacitors, *Adv. Energy Mater.*, 2015, **5**, 1401761, DOI: 10.1002/aenm.201401761.

48 X. Yang, *et al.*, Pore structure regulation of hierarchical porous carbon derived from coal tar pitch *via* pre-oxidation strategy for high-performance supercapacitor, *J. Colloid Interface Sci.*, 2022, **614**, 298–309, DOI: 10.1016/j.jcis.2022.01.093.

49 C. Liu, Y. Hou, Y. M. Li and H. I. Xiao, Heteroatom-doped porous carbon microspheres derived from ionic liquid-lignin solution for high performance supercapacitors, *J. Colloid Interface Sci.*, 2022, **614**, 566–573, DOI: 10.1016/j.jcis.2022.01.010.

50 Y. Lu, *et al.*, Hypercrosslinked polymers enabled micropore-dominant N, S Co-Doped porous carbon for ultrafast electron/ion transport supercapacitors, *Nano Energy*, 2019, **65**, 103993, DOI: 10.1016/j.nanoen.2019.103993.

51 H. Xu, Y. Zhang, L. Y. Wang, Y. Chen and S. Y. Gao, Hierarchical porous biomass-derived carbon framework with ultrahigh surface area for outstanding capacitance supercapacitor, *Renewable Energy*, 2021, **179**, 1826–1835, DOI: 10.1016/j.renene.2021.08.008.

52 T. S. Mathis, *et al.*, Energy Storage Data Reporting in Perspective—Guidelines for Interpreting the Performance of Electrochemical Energy Storage Systems, *Adv. Energy Mater.*, 2019, **9**, 1902007, DOI: 10.1002/aenm.201902007.

53 M. Nazarian-Samani, *et al.*, Rational hybrid modulation of P, N dual-doped holey graphene for high-performance supercapacitors, *J. Power Sources*, 2017, **372**, 286–296, DOI: 10.1016/j.jpowsour.2017.10.087.

54 L. Liu, R. Guo, X. Zhang, H. Wang and F. Ran, Preparation and electrochemical performance of nitrogen-doped multi-walled carbon nanotubes, *Chin. J. Power Sources*, 2018, **42**, 662–664.

55 L. X. Li, J. Tao, X. Geng and B. G. An, Preparation and Supercapacitor Performance of Nitrogen-Doped Carbon Nanotubes from Polyaniline Modification, *Acta Phys.-Chim. Sin.*, 2013, **29**, 111–116, DOI: 10.3866/PKU.WHXB201211091.

56 Y. X. Zhang, *et al.*, Template-free method for fabricating carbon nanotube combined with thin N-doped porous carbon composite for supercapacitor, *J. Mater. Sci.*, 2019, **54**, 6451–6460, DOI: 10.1007/s10853-018-03290-x.

57 X. Y. Fu, A. B. Chen, Y. F. Yu, S. L. Hou and L. Liu, Carbon Nanotube@N-Doped Mesoporous Carbon Composite Material for Supercapacitor Electrodes, *Chem. Asian J.*, 2019, **14**, 634–639, DOI: 10.1002/asia.201801865.

58 X. Li, *et al.*, Self-supporting activated carbon/carbon nanotube/reduced graphene oxide flexible electrode for high performance supercapacitor, *Carbon*, 2018, **129**, 236–244, DOI: 10.1016/j.carbon.2017.11.099.

59 Y. Xu, *et al.*, Synthesis of multiwall carbon nanotubes *via* an inert atmosphere absent autogenetic-pressure method for supercapacitor, *J. Energy Storage*, 2019, **26**, 100995, DOI: 10.1016/j.est.2019.100995.

60 X. Xiao, *et al.*, Hierarchical hollow-tubular porous carbon microtubes prepared *via* a mild method for supercapacitor electrode materials with high volumetric capacitance, *RSC Adv.*, 2022, **12**, 16257–16266, DOI: 10.1039/D2RA02141B.

61 J. Zhao, *et al.*, Enabling high-volumetric-energy-density supercapacitors: designing open, low-tortuosity heteroatom-doped porous carbon-tube bundle electrodes, *J. Mater. Chem. A*, 2017, **5**, 23085–23093, DOI: 10.1039/C7TA07010A.

62 R. A. Senthil, V. K. Yang, J. Q. Pan and Y. Z. Sun, A green and economical approach to derive biomass porous carbon from freely available feather finger grass flower for advanced symmetric supercapacitors, *J. Energy Storage*, 2021, **35**, 102287, DOI: 10.1016/j.est.2021.102287.

63 Y. Cao, *et al.*, Hollow carbon microtubes from kapok fiber: structural evolution and energy storage performance, *Sustainable Energy Fuels*, 2018, **2**, 455–465, DOI: 10.1039/C7SE00481H.

64 W. Jiang, *et al.*, Hollow-tubular porous carbon derived from cotton with high productivity for enhanced performance supercapacitor, *J. Power Sources*, 2019, **438**, 226936, DOI: 10.1016/j.jpowsour.2019.226936.

65 B. B. Liu, L. Wang, Y. Zhang, J. Du and A. B. Chen, Monomer self-deposition synthesis of N-doped mesoporous carbon tubes using halloysite as template for supercapacitors, *J. Mater. Sci.*, 2021, **56**, 3312–3324, DOI: 10.1007/s10853-020-05414-8.

66 P. Zuo, J. Du, Y. Yu and A. Chen, N-doped mesoporous thin carbon tubes obtained by exhaust directional deposition for supercapacitor, *Chem. Eng. Sci.*, 2021, **240**, 116651, DOI: 10.1016/j.ces.2021.116651.